RSC Advances

PAPER

View Article Online
View Journal | View Issue

Cite this: *RSC Adv.*, 2020, **10**, 16323

Aerosol synthesis of TiO_2:Er^{3+}/Yb^{3+} submicron-sized spherical particles and upconversion optimization for application as anti-counterfeiting materials

Kyeong Youl Jung

Er^{3+}/Yb^{3+}-doped TiO_2 up-conversion (UC) phosphors were prepared by spray pyrolysis, and the UC luminescence properties were optimized by changing the calcination temperature and the concentration of Er^{3+} and Yb^{3+} dopants. TiO_2:Er^{3+}/Yb^{3+} showed green and red emissions due to the $^2H_{11/2}/^4S_{3/2} \rightarrow {}^4I_{15/2}$ transition and the $^4F_{9/2} \rightarrow {}^4I_{15/2}$ transition of Er^{3+} ions, respectively. The R/G ratio between red (R) and green (G) emissions does not change significantly with Er concentration but increases linearly with increasing Yb^{3+} concentration. The dependence of UC luminescence intensity on 980 nm IR pumping power showed that both the red and green UC luminescence of TiO_2:Er^{3+}/Yb^{3+} occurred through a typical two-photon process. In terms of achieving the highest red UC emission intensity, the optimal Er^{3+} and Yb^{3+} contents are 0.3% and 7.0%, respectively. The UC intensity of TiO_2:Er^{3+}/Yb^{3+} particles increases until they are calcined at temperatures up to 600 °C and then decreases rapidly above 800 °C. This is because when the calcination temperature is 800 °C and higher, not only does the phase transition of TiO_2:Er^{3+}/Yb^{3+} occur from anatase to rutile, but also the $Yb_2Ti_2O_7$ impurity phase is formed. According to SEM and TEM/EDX analysis, the prepared TiO_2:Er^{3+}/Yb^{3+} UC powders have an average particle size of 680 nm, a spherical shape with a dense structure, and Er and Yb are uniformly dispersed throughout the particles without local separation. A mark prepared using TiO_2:Er^{3+}/Yb^{3+} powder was found to have a UC emission high enough to be visually observed when irradiated with a portable 980 nm IR lamp.

Received 18th February 2020
Accepted 19th April 2020

DOI: 10.1039/d0ra01549k

rsc.li/rsc-advances

Introduction

The growth of the global economy and globalization of the market are accelerating the emergence of various functional products and devices. At the same time, the number of counterfeit products is increasing, and global companies are making great efforts to develop various anti-counterfeiting technologies.[1–3] The number of counterfeit banknotes, documents and gift certificates is steadily increasing and is a national issue beyond corporate and personal infringement. In particular, the forgery of unique marks or patterns that symbolize products is becoming increasingly sophisticated to the extent that it is difficult for the naked eye to distinguish it from the original. Therefore, the development of advanced anti-counterfeiting technology, which makes it difficult to duplicate and easy to distinguish genuine products from counterfeits, is becoming more important. Security technology utilizing optical materials has the advantage of being able to quickly and visually identify replicas.[4–7] Banknotes that emit certain patterns when illuminated with ultraviolet (UV) light are examples of typical luminescence-based security technology applications.[8,9] Luminescence includes down-conversion (DC), which converts high energy, such as ultraviolet light, into low-energy visible light, and up-conversion (UC), which absorbs low energy, such as near infrared (NIR), to emit visible light. Therefore, the security technology using the light emitting material has the advantage that it is easy to check the security information by using a variety of excitation energy sources to visually check the various emission colors.[10–12] In particular, the security technology using UC properties of rare earth doped materials can be distinguished from the existing anti-counterfeiting technology using UV-based DC materials and can be used as a new security technology.[13–15]

Red, green and blue up-conversion can be achieved in a variety of matrixes using Er^{3+}, Ho^{3+} and Tm^{3+} as activators and Yb^{3+} as deactivators.[16–18] The most commonly used host material is a fluorine compound such as $NaYF_4$.[19–21] In terms of chemical stability and simplicity of synthetic conditions, an oxide matrix is preferred to a fluorine matrix. Y_2O_3, Gd_2O_3, $GdVO_4$, CeO_2, ZrO_2, TiO_2, *etc.* have been studied as oxide matrix for UC phosphors.[22–27] Among them, TiO_2 has many advantages; it is relatively inexpensive due to abundant reserves, semi-

Department of Chemical Engineering, Kongju National University, 1224-24 Cheonan-Daero, Seobuk-gu, Cheonan, Chungnam 31080, Republic of Korea. E-mail: kyjung@kongju.ac.kr

conductive with having excellent photochemical stability, and low toxicity to human body. As a result, TiO_2 is used in various fields such as pearl pigments, sunscreen cosmetics, paints, catalysts, and solar cells.[28–35] TiO_2 is suitable as a UC phosphor matrix because of its low phonon energy (<700 cm^{-1}).[36] Thus, TiO_2 doped with Er^{3+} or Er^{3+}/Yb^{3+} is prepared as nanoparticles or thin films and used in solar cells and photocatalysts.[37,38] Despite the many advantages of TiO_2:Er/Yb with UC properties, studies on optical property optimization and application as security materials have not been carried out systematically.

Er^{3+}/Yb^{3+} doped TiO_2 emits green and red light. Its emission intensity and main emission color can be adjusted by controlling the Er^{3+}/Yb^{3+} molar ratio. Therefore, it is necessary to optimize the dopant concentration in order to make the luminescence intensity the highest with the color suitable for the purpose. TiO_2:Er^{3+}/Yb^{3+} luminescence properties are affected by the synthesis method. This is because the size, shape, crystal phase, crystallinity (crystal size), distribution of dopants in the particle, *etc.* of the phosphor particles vary depending on the synthesis method. In order for the phosphor powder to have excellent luminescence properties, the dopant of an appropriate concentration needs to be uniformly distributed throughout the host particle, and the crystallinity of the host matrix should be high without forming an impurity phase. Therefore, it is important to develop a suitable synthesis technology for the production of TiO_2-based phosphor having excellent light emission characteristics. Until recently, much of Er^{3+}/Yb^{3+} doped TiO_2 synthesis studies focused on the preparation of thin films or nanoparticles using the sol–gel method.[39–41] Spray pyrolysis is one of the representative aerosol vapour-phase synthesis methods. In the spray pyrolysis method, since the particles can be continuously synthesized from one droplet through drying/pyrolysis, the particles produced have a spherical shape with a fine and narrow particle size distribution. When the multicomponent compound is prepared by the spray pyrolysis process, high purity single crystallinity can be obtained without separating the phases of each component. As mentioned above, the dopant components in the phosphor should be well substituted into the parent crystal lattice. Thus, spray pyrolysis has been applied to the synthesis of various phosphors with multi-component compositions because dopants can be mixed with the parent at the molecular level.[42,43] Nevertheless, to the best of our knowledge, there are no studies on the production and emission characteristics of TiO_2 doped with Er^{3+}/Yb^{3+} using spray pyrolysis. In this study, TiO_2:Er^{3+}/Yb^{3+} microspheres were prepared by spray pyrolysis. The effect of Er^{3+} and Yb^{3+} concentration on the luminescence properties was investigated and the most appropriate composition was determined in terms of luminance intensity. The effect of post-heat treatment temperature on the crystal phase and optical properties of TiO_2:Er^{3+}/Yb^{3+} was investigated. Finally, by evaluating the logo fabricated using powders with optimized UC luminescence, the applicability of TiO_2:Er^{3+}/Yb^{3+} prepared by spray pyrolysis was evaluated.

Experimental

TiO_2 doped with Er^{3+}/Yb^{3+} was prepared using a spray pyrolysis process. Titanium(IV) isopropoxide (TTIP, Aldrich 97%), erbium oxide (Er_2O_3, Aldrich 99.9%), and ytterbium nitrate ($Yb(NO_3)_3$, Alfa Aesar 99.99%) were used as Ti, Er and Yb precursors, respectively. The spray pyrolysis apparatus consisted of an ultrasonic droplet generator with 17 ultrasonic oscillators of 1.7 MHz, a quartz tube with a diameter of 1200 mm and a diameter of 55 mm, and a Teflon bag filter. Er and Yb precursors were previously dissolved with nitric acid and distilled water and used as necessary. Spray solution for preparing $(Ti_{1-x-y}, Er_x, Yb_y)O_2$ powder was prepared by the following procedure. First, the necessary amounts of Er (x) and Yb (y) were taken from the previously prepared active solution and placed in a 1000 mL beaker, and distilled water was added so that the total solution volume was 500 mL. 20 mL of nitric acid was added to the solution, and TTIP was slowly added thereto and mixed quickly using a magnetic stirrer until a clear solution was obtained. Finally, distilled water was added to make the total aqueous solution 1000 mL. Total precursor concentration was fixed at 0.1 M. The prepared spray solution was converted into droplets through an ultrasonic droplet generator. The resulting droplets were injected with 30 L min^{-1} of air into a quartz reaction tube maintained at 900 °C. The precursor solid particles produced while passing through the reaction tube were collected using a Teflon filter mounted at the exit of the quartz tube and calcined at 500 to 1000 °C for 3 hours within a box-type electric furnace.

The crystal phase change of the prepared TiO_2:Er/Yb powder was observed through a diffraction pattern which was obtained using a X-ray diffractometer (XRD, Rigaku, Miniflex 600) at 2θ = 20–70° at a scan rate of 4° min^{-1}. UC emission spectra of the samples were measured using a 980 nm IR Laser (Optoenergy, PL980P330J) as excitation source using a fluorescence spectrometer (PerkinElmer, LS 55). The output current of the IR laser was varied from 150 to 500 mA, and the resulting emission spectrum was measured at a wavelength in the range of 400 to 800 nm. The diffused reflectance spectrum was measured using UV-vis spectrophotometer (Shimadzu UV-2450). Analysis of particle shape, microstructure and composition was carried out through scanning electron microscopy (SEM) and transmission electron microscopy (TEM) analysis, supported by the Korea Basic Science Institute (KBSI).

Results and discussion

Fig. 1 shows the UC emission spectrum of TiO_2:Er^{3+} (0.5%) and TiO_2:Er^{3+}/Yb^{3+} (0.5%/1%) powder. The luminescence peaks observed are due to the $^2H_{11/2} \rightarrow {}^4I_{15/2}$ (535 nm), $^4S_{3/2} \rightarrow {}^4I_{15/2}$ (555 nm), and $^4F_{9/2} \rightarrow {}^4I_{15/2}$ (665 nm) transitions of Er^{3+} active ions. When Yb^{3+} is co-doped compared with the case where only Er^{3+} is doped, UC emission intensity is significantly improved. Yb^{3+} has a much larger light absorption cross-section area than Er^{3+}. Therefore, Yb^{3+} can more effectively absorb the incident IR light. The UC enhancement due to the co-doping means that the light energy absorbed by Yb^{3+} ions was effectively transferred to Er^{3+}. Er^{3+}/Yb^{3+}-doped TiO_2 has high emission intensity in both green and red. The red/green emission intensity depends on how energy transfer occurs from Yb^{3+} to Er^{3+}, which can vary greatly depending on the concentration of Er^{3+} and Yb^{3+}. Thus,

TiO_2:Er^{3+}/Yb^{3+} UC phosphors were prepared with varying concentrations of Er^{3+} and Yb^{3+}, and their UC properties were investigated.

Fig. 2 shows UC luminescence properties of samples prepared by varying Er^{3+} and Yb^{3+} concentrations. Fig. 2(a) is UC spectra observed with increasing Er^{3+} content from 0.01% to 1.25% at a fixed Yb^{3+} (1%). Both green and red UC emissions are highest at the Er^{3+} concentration of 0.3% and then gradually decrease above 0.5%. The relative peak intensity between green and red emission did not change significantly by the change in Er^{3+} concentration. TiO_2:Er^{3+}/Yb^{3+} samples were prepared with increasing concentrations of Yb^{3+} from 1% to 8% at an Er^{3+} concentration of 0.3%, and their UC spectra are shown in Fig. 2(b). The red UC intensity increases greatly and steadily with increasing Yb^{3+} concentration up to 7%. In contrast, when the Yb^{3+} concentration changes, the green UC intensity does not change significantly compared to the red UC emission, and the maximum is when the Yb^{3+} concentration is 3%. The ratios of red to green emission intensity (R/G) are shown as a function of Er^{3+} concentration in Fig. 2(c) and as a function of Yb^{3+} concentration in Fig. 2(d). The change in the R/G ratio with the Er^{3+} concentration is limited between 1.0 and 1.4, while the change in the R/G ratio with the Yb^{3+} concentration changes linearly. These results indicate that the $^4F_{9/2} \rightarrow {}^4I_{15/2}$ transition of Er^{3+} is more accelerated in the TiO_2 matrix than the $^2H_{11/2}/{}^4S_{3/2} \rightarrow {}^4I_{15/2}$ transition as the Yb^{3+} concentration increases. From the above results, it was concluded that the main UC emission color of TiO_2:Er^{3+}/Yb^{3+} phosphors was controlled by Yb^{3+} concentration rather than Er^{3+} concentration, and that the most appropriate Er^{3+} and Yb^{3+} concentrations in terms of red UC emission intensity were 0.3% and 7.0%, respectively.

Fig. 3 is a schematic diagram showing each energy level of Er^{3+} and Yb^{3+} and the UC luminescence mechanism. When only

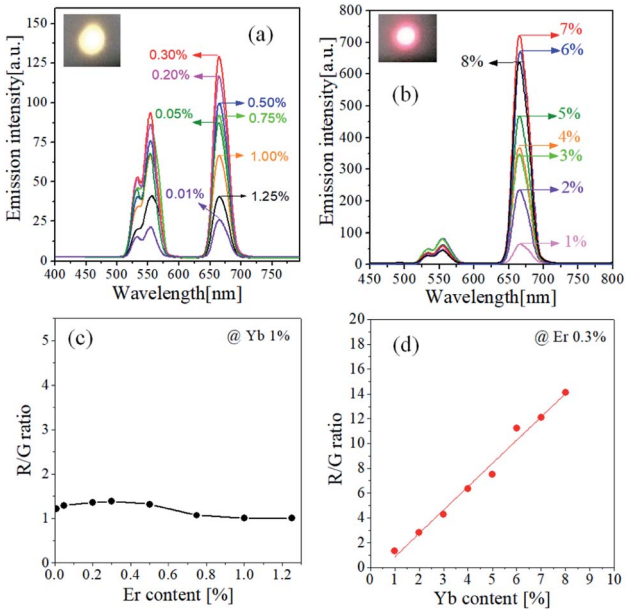

Fig. 2 UC spectra of TiO_2:Er^{3+}/Yb^{3+} samples prepared at different concentrations of Er^{3+} (a) and Yb^{3+} (b). R/G ratio as a function of the content of Er^{3+} (c) and Yb^{3+} (d).

Er^{3+} is doped, the electrons in the ground state are excited from $^4I_{15/2}$ to $^4I_{11/2}$ energy levels through ground state absorption (GSA). Photo-excited electrons at the $^4I_{11/2}$ energy level are consumed through two different ways. First they are directly excited to the $^4F_{7/2}$ level by excited state absorption (ESA) and followed by the non-radiative decay to the $^2H_{11/2}$ and $^4S_{3/2}$ energy levels by multi-phonon relaxation (MPR). Thereafter, they return to the ground state $^4I_{15/2}$, emitting green light. The second is that some of the photo-excited electrons at the $^4I_{11/2}$ level are transferred to the $^4I_{13/2}$ energy level by the MPR process, excited again to the $^4F_{9/2}$ level by the ESA process, and return to the ground state with red light emission. When the activator Er^{3+} coexists with Yb^{3+}, the UC luminescence mechanism depends on how energy transfer between Yb^{3+} and Er^{3+}

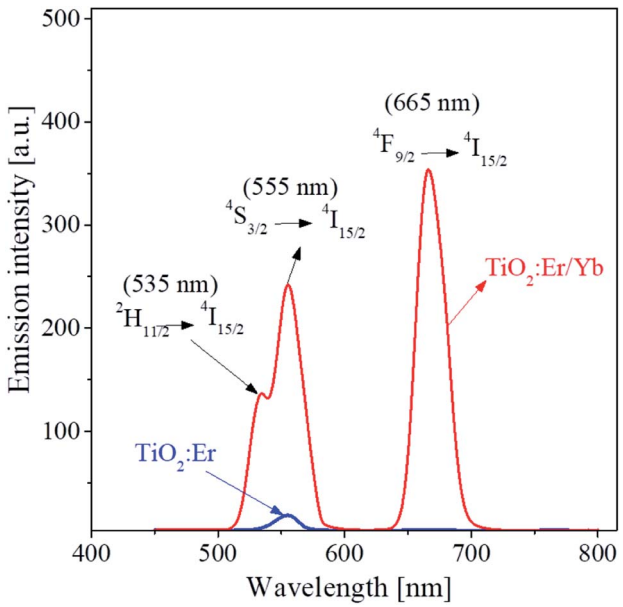

Fig. 1 UC emission spectra of TiO_2:Er^{3+} and TiO_2:Er^{3+}/Yb^{3+} particles prepared by spray pyrolysis.

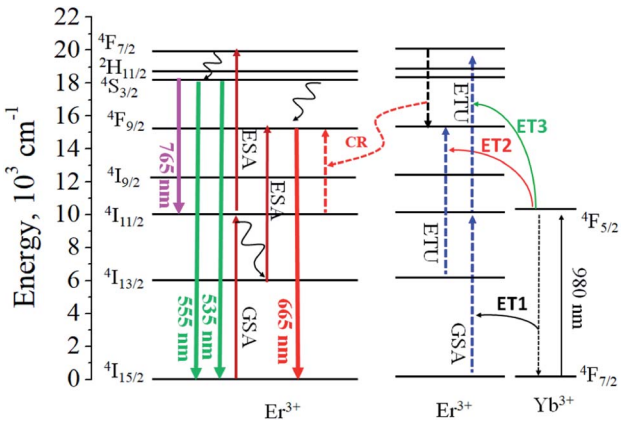

Fig. 3 Schematic diagram showing the energy level of each Er^{3+} and Yb^{3+} ion in TiO_2.

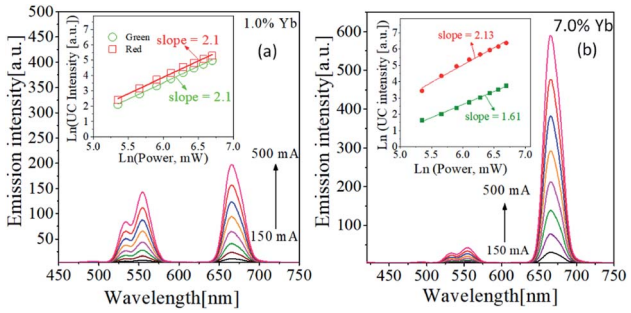

Fig. 4 Dependence of UC emission on IR pumping power for TiO_2:Er^{3+}/Yb^{3+} samples with different Yb^{3+} content, (a) 1.0% and (b) 7.0% under a fixed Er^{3+} content of 0.3%.

occurs. The IR absorption capability of Yb^{3+} is much greater than Er^{3+}. Also, since the Yb^{3+} concentration is much larger than the Er^{3+} concentration, most of the incident photons are absorbed by the Yb^{3+}, resulting in a $^4F_{7/2} \rightarrow {}^4F_{5/2}$ transition. Photoexcited electrons at $^4F_{5/2}$ of Yb^{3+} can transfer energy to Er^{3+} when returning to the ground state ($^4F_{7/2}$). Energy transfer from Yb^{3+} to Er^{3+} is possible in three ways, as indicated by ET1, ET2 and ET3 in Fig. 3. As shown in the experimental results (Fig. 2), the red emission intensity of TiO_2:Er^{3+}/Yb^{3+} increases with increasing Yb^{3+} concentration. This means that as the concentration of Yb^{3+} increases, photoelectrons are more filled in $^4F_{9/2}$ of Er^{3+}, which is an energy level capable of emitting red light. The increase of the photon concentration in the $^4F_{9/2}$ energy level of Er^{3+} can be achieved by the energy transfer paths including (1) ET2, (2) ET3 + MPR ($^4F_{7/2} \rightarrow {}^4F_{9/2}$), and (3) cross relaxation (CR) between two adjacent activators, $^4F_{7/2}$ (Er^{3+}) + $^4I_{11/2}$ (Er^{3+}) $\rightarrow$ $2\,^4F_{9/2}$ (Er^{3+}).

The dependence of the UC emission spectrum on IR light power was evaluated to determine the number of photons involved in green or red light emission. To use UC phosphors as a security material, the higher the emission intensity, the better. Also, the R/G ratio was largely changed by the Yb^{3+} content. Thus, two TiO_2:Er/Yb samples showing the maximum UC intensity in green (small R/G ratio) or red emission (large R/G ratio) were selected to investigate the IR power dependence. Fig. 4 shows the emission spectra observed with varying 980 nm IR power for samples with Yb^{3+} concentrations of 1% and 7% at the Er^{3+} concentrations of 0.3%. The relationship between the UC emission intensity (I) and the IR pumping power (P) is expressed by $I \propto P^n$, where n is the total number of photons participating in luminescence. When ln(I) is expressed as a function of ln(P), the value of n can be found from the slope. The relationship between ln(I) and ln(P) based on the intensity of each green and red UC emission peak in the measured emission spectrum is shown in the inset of Fig. 4. For red UC emission, the n values of samples with Yb^{3+} concentrations of 1% and 7% are 2.10 and 2.13, respectively. For green emission, the value of n is 2.10 for 1% Yb^{3+} and 1.61 for 7.0%. Table 1 shows the R/G ratios and n values of TiO_2:Er^{3+}/Yb^{3+} phosphors with different Er^{3+} and Yb^{3+} concentrations. The n value for red light emission has a value of about 2 and there is no big change

Table 1 Summary for the R/G ratio in UC emission and the n values in the IR power dependency for TiO_2:Er^{3+}/Yb^{3+}

				n value		
Er%	Yb%	Yb/Er ratio	R/G ratio	Green	Red	Ref.
0.05	1	20.0	1.3	1.97	1.92	This work
0.2	1	5.00	1.4	2.06	2.05	This work
0.3	1	3.33	1.4	2.13	2.13	This work
0.5	1	2.00	1.3	1.95	2.01	This work
0.3	3	10.00	4.3	1.88	2.17	This work
0.3	5	16.67	7.5	1.78	2.15	This work
0.3	7	23.33	12.0	1.61	2.12	This work
2	0	0	—	1.83	1.68	27
0.75	0	0	0.77	2.00	1.96	44
0.75	0.25	0.33	1.0	1.96	1.81	44
10	10	1.00	3–4	1.95	1.52	45
1	5	5.00	13	1.56	1.66	46

as the Yb^{3+} concentration increases. This result means that all red light emission is caused by two photon process regardless of Yb^{3+} concentration. The n value for green light emission gradually decreases from 2.10 (1%) to 1.61 (7%) with increasing Yb^{3+} concentration. At a fixed Yb^{3+} concentration (1%), the n values are close to 2.0 for both green and red UC emissions, indicating that there is no big change in the UC pathway by changing the Er^{3+} concentration. Referring to the previous reports on TiO_2:Er^{3+}/Yb^{3+} summarized in Table 1,[27,44–46] the higher the Yb^{3+}/Er^{3+} ratio, the higher the R/G ratio. This tendency is in good agreement with the results obtained in this work.

The minimum number of photons needed to generate visible light through absorption of 980 nm IR light is usually 2 in high efficiency UC phosphors. As shown in Table 1, the n value can be smaller than 2.0. According to Lei *et al.*,[47] whether $n = 1$ or 2 is determined by the depletion mechanism of photo-excited electrons at the intermediate energy level of UC emission. If photons at the intermediate energy level are dominantly depleted due to an upconversion process, $n = 1$, and $n = 2$ if they are dominantly depleted due to a linear decay. The n value can be between 1 and 2 if upconversion and linear decay occur competitively. The intermediate energy level of green UC emission is $^4I_{11/2}$. Experimental results show that when the Yb^{3+} concentration is low, the n values for green and red UC

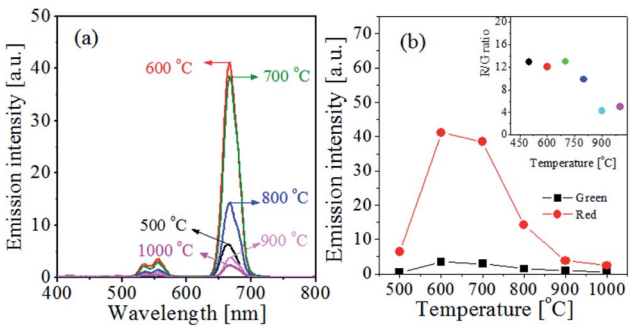

Fig. 5 (a) UC emission spectra and (b) the UC intensity of green and red for TiO_2:Er^{3+}/Yb^{3+} particles with different calcination temperature.

luminescence are close to 2 regardless of the Er^{3+} concentration change. This means that depletion of photons at intermediate energy levels for each emission is caused by linear decay. On the other hand, as the concentration of Yb^{3+} increases, energy transfer from Yb^{3+} to Er^{3+} can increase through the ET3 process ($^4I_{11/2} \rightarrow {}^4F_{7/2}$ transition) and the cross relaxation process ($^4I_{11/2} \rightarrow {}^4F_{9/2}$ transition). As a result, the main depletion of photons at the $^4I_{11/2}$ energy level can be upconversion and n should be close to 1. However, even when the Yb^{3+} concentration is 7%, $n = 1.61$ for green emission, indicating upconversion and linear decay are competitively involved in the depletion of photons at the $^4I_{11/2}$ level.

TiO_2 has a phase transition from anatase to rutile as the heat treatment temperature increases. The as-prepared TiO_2:Er^{3+}/Yb^{3+} powder was calcined with increasing post-heat treatment temperature from 500 °C to 1000 °C, and UC luminescence properties were investigated. Fig. 5(a) shows the UC spectrum at different calcination temperatures and Fig. 5(b) shows the green and red UC intensity as a function of temperature. The red and green luminescence peaks were highest at 600 °C and sharply decreased above 800 °C. From this, the most suitable calcination temperature was determined to be 600 °C in terms of UC emission intensity. The inset of Fig. 5(b) shows the change in the R/G ratio with the change in the calcination temperature. Below 700 °C there is no significant change in R/G values. Above 800 °C, however, the R/G ratio decreased significantly. This means that the reduction in red UC emission intensity is more severe than green UC intensity at 800 °C or more.

Fig. 6 is the XRD pattern of TiO_2:Er^{3+}/Yb^{3+} (0.3%/7.0%) UC powder prepared by different post-heat treatments. In order to more accurately observe the degree of anatase/rutile phase formation, the main peak of each phase of the XRD spectrum is enlarged and shown in Fig. 6(b). At the post-treatment temperature from 500 °C to 700 °C, the anatase phase was formed. At 800 °C, the peaks for rutile phase and $Yb_2Ti_2O_7$ phase as well as the anatase phase were observed. When the calcination temperature was 900 °C and 1000 °C, the anatase phase disappeared completely and instead the rutile and $Yb_2Ti_2O_7$ (or $Er_2Ti_2O_7$) crystal phase was observed. Fig. 6(c)

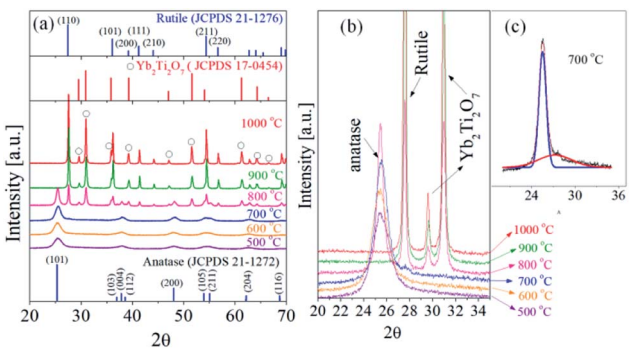

Fig. 6 (a) XRD pattern of TiO_2:Er^{3+}/Yb^{3+} UC powder prepared by different post-heat treatments. (b) Enlarged XRD patterns around the main peaks of anatase and rutile. (c) Peak deconvolution of XRD pattern for the sample calcined at 700 °C.

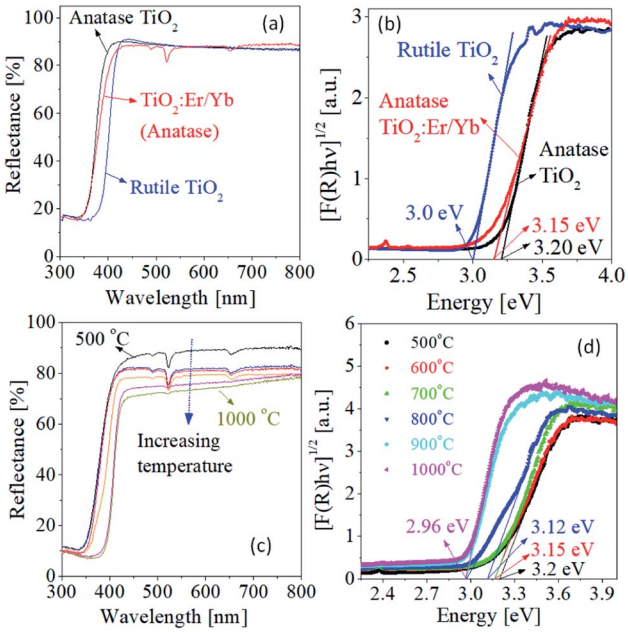

Fig. 7 UV/Vis reflectance spectra (a and c) and Tauc plots (b and d) for TiO_2:Er^{3+}/Yb^{3+} (0.3%/7.0%) particles prepared by spray pyrolysis and calcined at different temperatures.

shows an enlarged X-ray diffraction pattern between $2\theta = 20°$ to 35° for the sample heat-treated at 700 °C. The observed peak consists of a strong diffraction peak corresponding to the anatase phase and a weak diffraction peak corresponding to the rutile phase. This result indicates that the rutile phase is formed even when the heat treatment at 700 °C. Accordingly, the reason why the UC luminescence intensity of the sample heat-treated at 700 °C is slightly lower compared to the sample heat-treated at 600 °C is that rutile phase is formed. When the heat treatment temperature increased above 800 °C, Yb^{3+} was no longer substituted well in the host crystal lattice and involved in the formation of $Yb_2Ti_2O_7$ crystals. This means that Yb^{3+} no longer serves as a sensitizer in TiO_2:Er^{3+}/Yb^{3+}. Therefore, when the heat treatment temperature is 800 °C or more, the significant decrease in UC emission intensity is due to the formation of the $Yb_2Ti_2O_7$ phase together with the rutile phase formation.

Fig. 7(a) shows UV/visible reflectance for commercial TiO_2 (anatase and rutile) and TiO_2:Er^{3+}/Yb^{3+} powders prepared by spray pyrolysis. The Er^{3+}/Yb^{3+}-doped TiO_2 sample calcined at 600 °C have pure anatase as shown in Fig. 6. So, the overall reflectance spectrum of the Er^{3+}/Yb^{3+}-doped TiO_2 sample is similar with anatase TiO_2 with no dopants. Instead, unlike pure anatase TiO_2, the absorption edge of the Er^{3+}/Yb^{3+}-doped TiO_2 sample is located closer to the rutile TiO_2. For the TiO_2:Er^{3+}/Yb^{3+} sample, three absorption peaks are observed at 489 nm, 523 nm and 654 nm. This is the result of excitation of Er^{3+} ions substituted into the TiO_2 lattice from $^4I_{15/2}$ to $^4F_2$ (489 nm), $^2H_{11/2}$ (523 nm) and $^4F_{9/2}$ (654 nm) energy levels through light absorption. To determine the band gap of TiO_2 and Er^{3+}/Yb^{3+}-doped TiO_2, the diffuse reflectance (R) was treated by the modified Kubelka–Munk function, $F(R) = (1 - R)^2/2R$. The

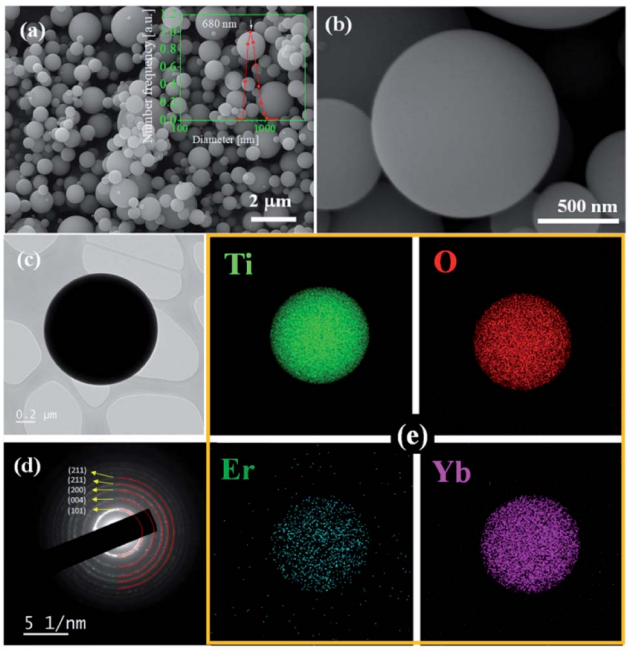

Fig. 8 SEM images (a and b), TEM (c), SAED pattern (d), and element mapping (e) for TiO_2:Er^{3+}/Yb^{3+} particles prepared by spray pyrolysis.

resulting $F(R)$ is proportional to absorption coefficient (α) and the band gap (E_g) can be estimated by the Tauc plot, $[F(R)h\nu]^n$ *versus* $h\nu$, where $n = 2$ for direct allowed transitions ad $n = 1/2$ for indirect allowed transition. TiO_2 is a semiconductor with an indirect band gap. Thus, the Tauc plot of $[F(R)h\nu]^{1/2}$ *versus* $h\nu$ was used to determine the band gap of TiO_2 or Er^{3+}/Yb^{3+}-doped TiO_2. As shown in Fig. 7(b), the band gaps of TiO_2 are 3.2 eV and 3.0 eV for anatase and rutile, respectively. TiO_2:Er^{3+}/Yb^{3+} with anatase phase has the band gap of about 3.15 eV. Fig. 7(c) shows the UV/visible reflectance for TiO_2:Er/Yb samples calcined at different temperatures, and the band gap was calculated through the Tauc plots shown in Fig. 7(d). The band gap of TiO_2:Er^{3+}/Yb^{3+} is progressively reduced from 3.2 eV to 2.96 eV when the calcination temperature increases from 500 °C to 1000 °C. At 800 °C, TiO_2:Er^{3+}/Yb^{3+} shows two band gaps of 3.12 eV and 2.96 eV due to the coexistence of anatase and rutile. In Fig. 7(c), the absorption peak at 523 nm due to the $^4I_{15/2} \rightarrow {}^2H_{11/2}$ transition of Er^{3+} is gradually reduced as the calcination temperature increases above 800 °C. This is because Er^{3+} or Yb^{3+} ions participate in the formation of $Er_2Ti_2O_7$ or $Yb_2Ti_2O_7$ crystals rather than being substituted into the TiO_2 lattice when the calcination temperature is over 800 °C.

Fig. 8 shows SEM/TEM images, SAED (Selected Area Electron Diffraction) pattern and element mapping results of TiO_2:Er^{3+}/Yb^{3+} UC powders prepared by spray pyrolysis and heat-treated at 600 °C. The prepared powder has a spherical shape. The inset of Fig. 8(a) shows the particle size distribution. The TiO_2:Er^{3+}/Yb^{3+} UC powders prepared have an average size of 680 nm and a narrow particle size distribution. As shown in Fig. 7(c), the TEM result that the TiO_2:Er^{3+}/Yb^{3+} particles prepared have a spherical shape with a dense structure. Fig. 8(d) is a SAED pattern for TiO_2:Er^{3+}/Yb^{3+} (0.3%/7.0%) prepared by spray pyrolysis and calcined at 600 °C. The rings observed are in good agreement with TiO_2 structure. The diffraction plane of each ring is shown in the image. The strongest diffraction ring is corresponding to the (101) plane of anatase TiO_2. Thus, the observed SAED pattern indicates that the TiO_2:Er^{3+}/Yb^{3+} particles prepared are typical nanocrystalline anatase polycrystals, which is in good agreement with the XRD results. Dopants should be well substituted in the host crystal lattice to obtain good UC luminescence. In order to confirm the distribution of the dopant in the TiO_2 matrix, element mapping for Ti, Er and Yb components was performed and the results are shown in Fig. 8(e). Er and Yb ions are uniformly distributed throughout the TiO_2 particle without local separation. Thus, the TiO_2:Er^{3+}/Yb^{3+} UC powder prepared by spray pyrolysis was found to have a dense, spherical shape, and dopants were well distributed throughout the host matrix. To see the applicability of TiO_2:Er^{3+}/Yb^{3+} as an emissive security material, the logo mark was prepared and the result is shown in Fig. 9. In natural light, the logo is white, a typical TiO_2 color. When illuminated with 980 nm IR light, this white logo emits strong UC light that is easily visible to the naked eye. Therefore, TiO_2:Er^{3+}/Yb^{3+} UC powder prepared by spray pyrolysis can be successfully used as a security material.

Fig. 9 KNU Log mark prepared using the optimized TiO_2:Er^{3+}/Yb^{3+} spherical particles under natural light (left) and when irradiating with a portable 980 nm IR lamp (right).

Conclusions

Submicron sized TiO_2:Er^{3+}/Yb^{3+} spherical particles were prepared by spray pyrolysis. The upconversion (UC) characteristics of the prepared TiO_2:Er^{3+}/Yb^{3+} were investigated with varying calcination temperature and Er and Yb contents. The prepared TiO_2:Er^{3+}/Yb^{3+} showed strong green and red UC emission at low Yb^{3+} concentrations. However, as the Yb^{3+} concentration increased, red emission improved much more than green emission. As a result, the ratio of red to green emission increased linearly with increasing Yb^{3+} content. According to the dependence of the UC emission on the IR pumping power, the UC emission of TiO_2:Er^{3+}/Yb^{3+} was found to be achieved by a typical two-photon process. When TiO_2:Er^{3+}/Yb^{3+} particles were synthesized by spray pyrolysis, in terms of obtaining the highest red emission, the optimum Er^{3+} and Yb^{3+} contents were found to be 0.3% and 7.0%, respectively. Also, the optimum calcination temperature for obtaining the highest UC emission intensity was 600 °C. Above 700 °C, a large decrease in UC strength was observed due to the formation of the rutile phase as well as the formation of the $Yb_2Ti_2O_7$ crystal phase. The prepared TiO_2:Er^{3+}/Yb^{3+} was a spherical particle with a dense structure and an average particle size of 680 nm. Finally,

it was confirmed that submicron-sized TiO_2:Er^{3+}/Yb^{3+} particles with optimized UC luminescence properties by spray pyrolysis can successfully act as security materials.

Conflicts of interest

There are no conflicts to declare.

Acknowledgements

This research was supported by Basic Science Research Program through the National Research Foundation of Korea (NRF) funded by the Ministry of Education (grant number: 2018R1D1A3B07049692). Kyeong Youl Jung would like to give special thanks to Professor Moo-Yeal Lee of the Department of Chemical and Biomolecular Engineering at Cleveland State University for his help in conducting this research.

Notes and references

1 K. Jiang, L. Zhang, J. Lu, C. Xu, C. Cai and H. Lin, *Angew. Chem., Int. Ed.*, 2016, **55**, 7231–7235.
2 Y. Cui, I. Y. Phang, Y. H. Lee, M. R. Lee, Q. Zhang and X. Y. Ling, *Chem. Commun.*, 2015, **51**, 5363–5366.
3 M. You, M. Lin, S. Wang, X. Wang, G. Zhang, Y. Hong, Y. Dong, G. Jin and F. Xu, *Nanoscale*, 2016, **8**, 10096–10104.
4 S. Berthier, J. Boulenguez and Z. Bálint, *Appl. Phys. A*, 2007, **86**, 123–130.
5 I.-H. Lee, G. Li, B.-Y. Lee, S.-U. Kim, B. Lee, S.-H. Oh and S.-D. Lee, *Opt. Express*, 2019, **27**, 24512–24523.
6 Y. Cui, R. S. Hegde, I. Y. Phang, H. K. Lee and X. Y. Ling, *Nanoscale*, 2014, **6**, 282–288.
7 P. Kumar, S. Singh and B. K. Gupta, *Nanoscale*, 2016, **8**, 14297–14340.
8 Q. Wang, J. Cai, K. Chen, X. Liu and L. Zhang, *Macromol. Mater. Eng.*, 2016, **301**, 337–382.
9 B. Song, H. Wang, Y. Zhong, B. Chu, Y. Su and Y. He, *Nanoscale*, 2018, **10**, 1617–1621.
10 S. Xie, G. Gong, Y. Song, H. Tan, C. Zhang, N. Li, Y. Zhang, L. Xu, J. Xu and J. Zheng, *Dalton Trans.*, 2019, **48**, 6971–6983.
11 X. Liu, Y. Wang, X. Li, Z. Yu, R. Deng, L. Liang, X. Xie, D. T. B. Loong, S. Song, D. Fan, A. H. All, H. Zhang, L. Huang and X. Liu, *Nat. Commum.*, 2017, **8**, 899.
12 W. Yao, Q. Tian, J. Liu, Q. Xue, M. Li, L. Liu, Q. Lu and W. Wu, *Nanoscale*, 2017, **9**, 15982–15989.
13 H. Tan, G. Gong, S. Xie, Y. Song, C. Zhang, N. Li, D. Zhang, L. Xu, J. Xu and J. Zheng, *Langmuir*, 2019, **35**, 11503–11511.
14 J. Xu, B. Zhang, L. Jia, Y. Fan, R. Chen, T. Zhu and B. Liu, *ACS Appl. Mater. Interfaces*, 2019, **11**, 38.
15 M. Rao, J. Fu, X. Wen, B. Sun, J. Wu, X. Liu and X. Dong, *New J. Chem.*, 2018, **42**, 12353–12356.
16 A. S. Gouveia-Neto, L. A. Bueno, R. F. do Nascimento, E. A. da Silva Jr and E. B. da Costa, *Appl. Phys. Lett.*, 2007, **91**, 091114.
17 J. Yang, C. Zhang, C. Peng, C. Li, L. Wang, R. Chai and J. Lin, *Chem.–Eur. J.*, 2009, **15**, 4649–4655.
18 J. M. Meruga, A. Baride, W. Cross, J. J. Kellar and P. S. May, *J. Mater. Chem. C*, 2014, **2**, 2221–2227.
19 J.-C. Boyer, L. A. Cuccia and J. A. Capobianco, *Nano Lett.*, 2007, **7**, 847–852.
20 C. F. Gainer, G. S. Joshua, C. R. De Silva and M. Romanowski, *J. Mater. Chem.*, 2011, **21**, 18530–18533.
21 E. He, J. Yu, C. Wang, Y. Jiang, X. Zuo, B. Xu, J. Wen, Y. Qin and Z. Wang, *Mater. Res. Bull.*, 2020, **121**, 110613.
22 X. Yang, M. Liu, J. Liu, Y. Xia, W. Ji, Z. Li, J. Chen, L. Liu, L. Hao, B. Dong, S. Agathopoulos and X. Xu, *Phys. Chem. Chem. Phys.*, 2020, **22**, 2819–2826.
23 A. Kumar, S. P. Tiwari, K. Kumar and V. K. Rai, *Spectrochim. Acta, Part A*, 2016, **167**, 134–141.
24 K. Y. Jung, B. Ho. Min, D. S. Kim and B.-K. Choi, *Curr. Opt. Photonics*, 2019, **3**, 248–255.
25 B. H. Min and K. Y. Jung, *RSC Adv.*, 2019, **9**, 20002–20008.
26 L. Liu, Y. Wang, X. Zhang, K. Yang, Y. Bai, C. Huang and Y. Song, *Opt. Commun.*, 2011, **284**, 1876–1879.
27 J. Zhang, X. Wang, W.-T. Zheng, X.-G. Kong, Y.-J. Sun and X. Wang, *Mater. Lett.*, 2007, **61**, 1658–1661.
28 Q. Gao, X. Wu, Y. Fan and X. Zhou, *Dyes Pigm.*, 2012, **95**, 534–539.
29 M. Morsella, N. d'Alessandro, A. E. Lanterna and J. C. Scaiano, *ACS Omega*, 2016, **1**, 464–469.
30 A. Al-Kattan, A. Wichser, S. Zuin, Y. Arroyo, L. Golanski, A. Ulrich and B. Nowark, *Environ. Sci. Technol.*, 2014, **48**, 6710–6718.
31 S. P. Hong, S. Kim, N. Kim, J. Yoon and C. Kim, *Korean J. Chem. Eng.*, 2019, **36**, 1753–1766.
32 K. Y. Jung, S. B. Park and S.-K. Ihm, *Appl. Catal., B*, 2004, **51**, 239–245.
33 J. M. Won, M. S. Kim and S. C. Hong, *Korean J. Chem. Eng.*, 2018, **35**, 2365–2378.
34 J. Choi, K. S. Yoo and J. Kim, *Korean J. Chem. Eng.*, 2018, **35**, 2481–2486.
35 J. Y. Oh, S. A. Song, K. Y. Jung, Y.-W. Chang, K. Kim, S. N. Lim and Y.-C. Jeong, *Electrochim. Acta*, 2017, **253**, 390–395.
36 A. Bahtat, M. Bouazaoui, M. Bahtat and J. Mugnier, *Opt. Commun.*, 1994, **111**, 55–60.
37 X. Wang, Z. Zhang, J. Qin, W. Shi, Y. Liu, H. Gao and Y. Mao, *Electrochim. Acta*, 2017, **245**, 839–845.
38 J. Reszczyńska, T. Grzyb, J. W. Sobczak, W. Lisowski, M. Gazda, B. Ohtani and Z. Zaleska, *Appl. Catal., B*, 2015, **163**, 40–49.
39 M. Jiang, C. Zhu, J. Zhou, J. Chen, Y. Gao, X. Ma and D. Yang, *J. Appl. Phys.*, 2016, **120**, 163104.
40 B. S. Cao, Y. Y. He, Z. Q. Feng, M. Song and B. Dong, *Opt. Commun.*, 2011, **284**, 3311–3314.
41 Y. Wu, S. Lin, J. Liu, Y. Ji, J. Xu, L. Xu and K. Chen, *Opt. Express*, 2017, **25**, 22648–22657.
42 B. H. Min and K. Y. Jung, *RSC Adv.*, 2017, **7**, 44759–44765.
43 K. Y. Jung, J. C. Lee, D. S. Kim, B.-K. Choi and W.-J. Kang, *J. Lumin.*, 2017, **192**, 1313–1321.
44 W. Luo, C. Fu, R. Li, Y. Liu, H. Zhu and X. Chen, *Small*, 2011, **7**, 3046–3056.
45 Q. Shang, H. Yu, X. Kong, H. Wang, X. Wang, Y. Sun, Y. Zhang and Q. Zeng, *J. Lumin.*, 2008, **128**, 1211–1216.
46 Z. Zhang, J. Zhang, W. Zhou, M. Song, W. Li, Q. Hu and X. Zhao, *Adv. Mater. Res.*, 2009, **66**, 1662–8985.
47 Y. Lei, H. Song, L. Yang, L. Yu, Z. Liu, G. Pan, X. Bai and L. Fan, *J. Chem. Phys.*, 2005, **123**, 174710.